



**POLITECNICO**  
MILANO 1863

SCUOLA DI INGEGNERIA INDUSTRIALE  
E DELL'INFORMAZIONE

EXECUTIVE SUMMARY OF THE THESIS

## Developing a Performance Tool for Bistatic Repeat-Pass SAR Interferometry

LAUREA MAGISTRALE IN SPACE ENGINEERING - INGEGNERIA SPAZIALE

**Author:** LEONARDO MANISCALCO

**Advisor:** PROF. STEFANO TEBALDINI

**Academic year:** 2022-2023

### 1. Introduction

The SAOCOM-CS Mission marks a decade-long collaboration among scientists and engineers globally, responding to the Argentina National Commission on Space Activities' invitation [1]. This initiative birthed various projects about a cost-effective bistatic Synthetic Aperture Radar (SAR) receiver, surpassing conventional SAR implementations in information content.

Leveraging this success, this work introduces an innovative system bridging current and future SAR missions, with a design similar to the PAR-SIFAL proposal [4]. Key objectives include precise measurements of North along-track deformation vectors, particularly in the Cryosphere, and accurate measurements of the deformation rates.

Beyond primary goals, the system promises unprecedented products through bistatic technology. As Earth faces increasing human-induced changes, this work emphasizes the critical role of understanding biosphere and cryosphere characteristics, positioning the proposed system as a pioneering tool for advancing environmental insights and contributing to global sustainability. Furthermore, a newly devised **performance tool** has been created to evaluate the various

accuracies. This tool enables engineers and mission designers to quickly identify the optimal parameter combination for each scenario, enhancing the efficiency of the SAR system and ensuring its optimal performance in diverse environmental conditions.

### 2. DInSAR and BiSAR: Principles and Challenges

**SAR** technology, a radar-based remote sensing method, is crucial for high-resolution Earth surface imaging [2]. In Equations 1, the fundamental Azimuth resolution  $\Delta x$ , slant range resolution  $\Delta R$ , and ground resolution  $\Delta R_{gr}$  formulas are provided.

$$\Delta x = \frac{L_x}{2}, \quad \Delta R = \frac{c}{2B_w}, \quad \Delta R_{gr} = \frac{\Delta R}{\sin \theta} \quad (1)$$

The **Differential Interferometric Synthetic Aperture Radar (DInSAR)** technique has various applications and presents numerous advantages and challenges. One of its well-recognized primary constraints stems from the characteristic near-polar orbits of DInSAR, as illustrated in Figure 1, commonly referred to as the North-South problem. Apart from this, DInSAR emerges as a pivotal technology offering

millimeter-scale precision in detecting ground movements, enabling large-scale coverage and temporal monitoring. Applications span geo-hazard monitoring, subsidence analysis, infrastructure stability assessment, and environmental monitoring.

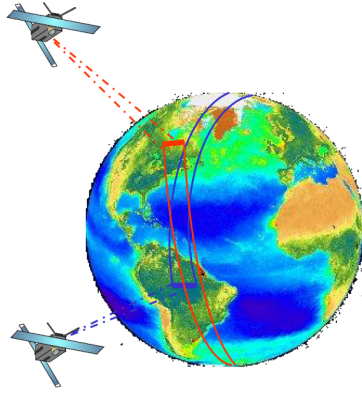


Figure 1: Typical DInSAR satellite orbits. It can be noted that are nearly polar orbit, thus with  $i \approx 90^\circ$ .

The **North-South problem**, a challenge in SAR-based deformation monitoring, is meticulously explored. The limitation in accurately measuring the North component of the deformation vector, especially in nearly polar satellite orbits, poses challenges in scenarios like faults, volcanic zone monitoring, and ice surface velocity tracking. Current methods, including offset tracking and innovative solutions like the SENTINEL-1 satellite's TOPS acquisition methodology, are considered.

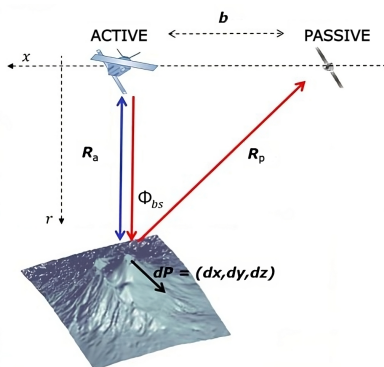


Figure 2: Typical along-track SAR Bistatic configuration, used in this work.

An intelligent way to address the North-South problem is by delving into the domain of **Bistatic Synthetic Aperture Radar**, or

BiSAR. This innovative configuration, shown in Figure 2, with a physically separated transmitter and receiver, offers a flexible geometry, diverse baseline angles, and enhanced target identification capabilities. The advantages, challenges, and applications of BiSAR are discussed, setting the stage for detailed exploration in subsequent chapters. In this work, a bistatic angle of  $\phi_{bs} = 20^\circ$  is used.

The significance of the chosen L-band for BiSAR missions, exemplified by the innovative PARSIFAL proposal [4], is underlined. L-Band was chosen for its superior ability to penetrate ice and forests, maintain fine spatial resolution, and reduce temporal decorrelation effects. The central frequency used in this work is  $f = 1.275$  GHz, while the bandwidth is  $B_w = 35.5$  MHz.

### 3. Error Sources and Challenges

At this point, a critical assessment of **error sources** in a bistatic InSAR system is crucial for understanding and mitigating inaccuracies in measurements. The primary focus is on easily addressable error sources such as clock error, orbital error, and residual topography, which, when effectively mitigated, contribute minimally to the overall error.

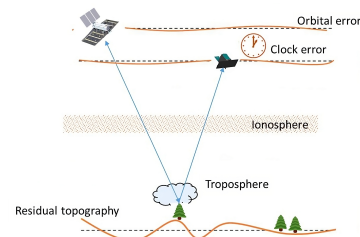


Figure 3: Visual Depiction of Phase Screens that contribute to the InSAR Phase.

Clock synchronization, essential for interferometric InSAR precision, is achieved through co-registering active and passive images, with methodologies demonstrated in previous studies. Notably, precision to the order of millimeters renders clock errors inconsequential for subsequent analysis.

Orbital errors, particularly phase screens arising from imperfect knowledge of satellite orbits, are mitigated using advanced correction algorithms, achieving high precision. The impact of decorrelation resulting from unavoidable **baselines** is

a nuanced aspect explored in detail.

Residual **topography**, uncorrected in some scenarios, can introduce bias into LoS deformation estimation. While current terrain models exhibit high accuracy, the presence of significant across-track baselines may necessitate careful consideration.

At this point, the focus can shift to the main sources of errors, highlighting the atmosphere and decorrelation-induced phase noise as the most significant ones. A covariance matrix,  $\mathbf{C}_\varepsilon$  (see Matrix 2), is introduced, serving as the foundation for the subsequent accuracy analysis.

$$\mathbf{C}_\varepsilon = \begin{bmatrix} \sigma_a^2 + \sigma_{\varphi,a}^2 & Cov(a,p) \\ Cov(a,p) & \sigma_p^2 + \sigma_{\varphi,p}^2 \end{bmatrix} \quad (2)$$

The atmosphere, composed of tropospheric and ionospheric layers, introduces phase variations influencing InSAR measurements.

$$\begin{cases} d\varphi_a = 2\varphi_{iono}^m + 2\varphi_{tropo}^m + 2\varphi_{turb}^m \\ d\varphi_p = \varphi_{iono}^m + \varphi_{tropo}^m + \varphi_{turb}^m \\ \quad + \varphi_{iono}^b + \varphi_{tropo}^b + \varphi_{turb}^b \end{cases} \quad (3)$$

A detailed mathematical model, shown in 3 and detailed in 4, considers non-turbulent and turbulent layers in the troposphere, as well as ionospheric effects. The spatial correlation  $\rho$  of phase screens is crucial in assessing accuracy.

$$\begin{cases} \sigma_a^2 = E[(d\varphi_a)^2] = \sigma_{iono}^2 + \sigma_{tropo}^2 + \sigma_{turb}^2 \\ \sigma_p^2 = E[(d\varphi_p)^2] = \frac{\sigma_{iono}^2}{2}(1 + \rho_{iono}) + \\ \quad + \frac{\sigma_{tropo}^2}{2}(1 + \rho_{tropo}) + \frac{\sigma_{turb}^2}{2}(1 + \rho_{turb}) \\ Cov(a,p) = E[d\varphi_a d\varphi_p] = \frac{\sigma_{iono}^2}{2}(1 + \rho_{iono}) + \\ \quad + \frac{\sigma_{tropo}^2}{2}(1 + \rho_{tropo}) + \frac{\sigma_{turb}^2}{2}(1 + \rho_{turb}) \end{cases} \quad (4)$$

The **decorrelation-induced phase noise**, obtained from the Cramér-Rao Bound in 5, serves as a theoretical lower limit for phase noise variance.

Its application in multi-looked interferograms provides valuable insights into the precision of phase estimates under noisy conditions.

$$\sigma_\varphi = \sqrt{\frac{1 - |\gamma|^2}{2L_{eq}|\gamma|^2}} \quad (5)$$

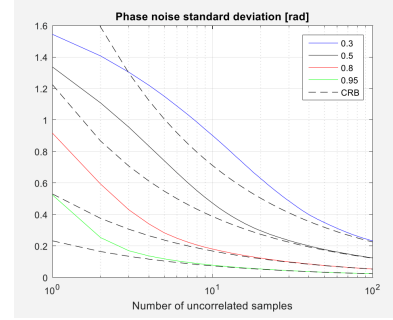


Figure 4: Cramér-Rao bound for different coherence values ( $\gamma$  in the legend).

## 4. Performance Model and Orbital Analysis

At this point, the mathematical foundations of bistatic DInSAR must be introduced, as well as some models associated with this advanced remote sensing technique. The primary focus lies in understanding the **North-East-Up** error covariance matrix (see the relative reference frame in Figure 5), which characterizes the statistical properties of the InSAR measurements.

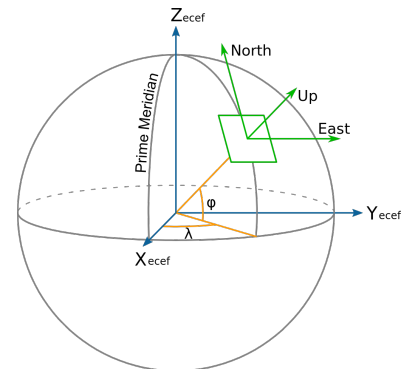


Figure 5: The North-East-Up coordinate system.

The focus is on the transformation from slant range measurements to ground displacement vectors in North, East, and Up components. As a first step, the relation 6 is written.

$$\begin{bmatrix} d\varphi_a \\ d\varphi_p \end{bmatrix} = \mathbf{A} \begin{bmatrix} dx \\ dr \end{bmatrix} + \varepsilon \quad (6)$$

where

$$\mathbf{A} = \begin{bmatrix} 0 & \frac{4\pi}{\lambda} \\ \frac{2\pi}{\lambda} \sin(\phi_{bs}) & \frac{2\pi}{\lambda} (1 + \cos(\phi_{bs})) \end{bmatrix}$$

Then, the  $dx-dr$  covariance matrix 7 can be obtained, exploiting the covariance matrix propa-

gation property.

$$\mathbf{C}_{dxdr} = \mathbf{A}^{-1} \mathbf{C}_\varepsilon (\mathbf{A}^{-1})^T \quad (7)$$

Now, putting together ascending and descending passages, the Matrix 8 is obtained.

$$\mathbf{C}_{dxdr}^* = \begin{bmatrix} \mathbf{C}_{dxdr}^{(as)} & \mathbf{0}_{[2 \times 2]} \\ \mathbf{0}_{[2 \times 2]} & \mathbf{C}_{dxdr}^{(ds)} \end{bmatrix} \quad (8)$$

Knowing finally the Relation 9 to go from  $dx-dr$  to NEU reference frame

$$\begin{bmatrix} dx_{as} \\ dr_{as} \\ dx_{ds} \\ dr_{ds} \end{bmatrix} = \mathbf{B} \begin{bmatrix} d_N \\ d_E \\ d_U \end{bmatrix} + \varepsilon \quad (9)$$

where

$$\mathbf{B} = \begin{bmatrix} \sin \psi_{as} & \cos \psi_{as} & 0 \\ -\cos \psi_{as} \sin \theta_{as} & \sin \psi_{as} \sin \theta_{as} & -\cos \theta_{as} \\ -\sin \psi_{ds} & \cos \psi_{ds} & 0 \\ -\cos \psi_{ds} \sin \theta_{ds} & -\sin \psi_{ds} \sin \theta_{ds} & -\cos \theta_{ds} \end{bmatrix}$$

the required covariance matrix 10 is found.

$$\mathbf{C}_{NEU} = \mathbf{B}^+ \mathbf{C}_{dxdr}^* (\mathbf{B}^+)^T \quad (10)$$

This critical covariance matrix, denoted as  $\mathbf{C}_{NEU}$ , encapsulates the uncertainties in these components. To extract meaningful insights, the diagonal of  $\mathbf{C}_{NEU}$  is scrutinized, unveiling the variances, hence the standard deviations, of measurements along the North, East, and Up directions.

Another important topic is interferometric coherence modeling, which can be thought of as the product of four coherence terms (see Equation 11): system, temporal, flat, and volumetric decorrelation. Each term is meticulously formulated, incorporating parameters like SNR, TAR, NESZ, terrain characteristics, and subsurface volume alterations.

$$\gamma = \gamma_{SNR} \cdot \gamma_{temp} \cdot \gamma_{flat} \cdot \gamma_{vol} \quad (11)$$

Finally, in the **orbital part**, the nearly polar orbit of the COSMO-SkyMed constellation, a pertinent choice for InSAR applications, is considered. The distinctive characteristics of this constellation, including orbit height, inclination, and revisit capability, are highlighted. Moreover, the spherical Earth model is incorporated for precise analysis, necessitating corrections for depression and grazing angles due

to Earth's curvature. An appropriate MATLAB function seamlessly translates off-nadir angles to incidence angles, crucial for aligning satellite observations with analysis requirements.

## 5. Single-Passage Performances

Established the mathematical framework, a comprehensive analysis of the single-pass performance of the bistatic InSAR system is carried out, particularly in the context of various scenarios and environmental conditions.

First of all, a scenario description is necessary. Four scenarios have been considered: Solid Earth, Cryosphere, Short Vegetation, and Landslides. Notably, the analysis considers scenarios with and without atmospheric effects, shedding light on the system's resilience in different environmental conditions.

The analysis uncovers nuanced patterns by meticulously examining **accuracy** plots in scenarios such as Solid Earth and Landslides. For instance, Figure 6 and Figure 7 depict plots illustrating the relationship between SNR and accuracy. The phase noise is found to have a relatively minor impact on accuracy.

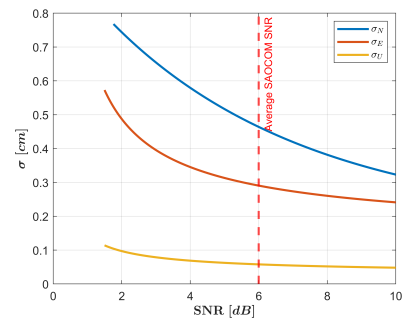


Figure 6: Accuracy in function of SNR, NO atmosphere, NO baseline - Solid Earth scenario.

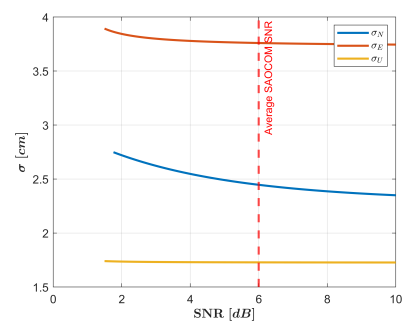


Figure 7: Accuracy in function of SNR, **with atmosphere, 200 m baseline** - Landslides scenario.

Further, the calculation of backscatter coefficients, a critical component in assessing system accuracy, is addressed. Leveraging a MATLAB script and the Handbook of Radar Scattering Statistics database [5], the mean backscatter coefficient can be calculated for every incidence angle needed.

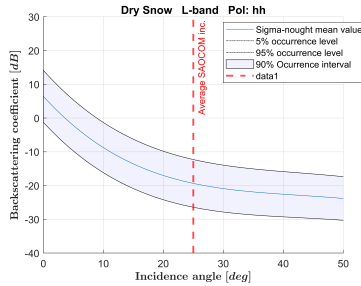


Figure 8: Cryosphere backscatter coefficient trend.

The introduction of atmospheric conditions introduces a trade-off in the incidence angle, highlighting the intricate balance among SNR, backscatter coefficients, and ground resolution.

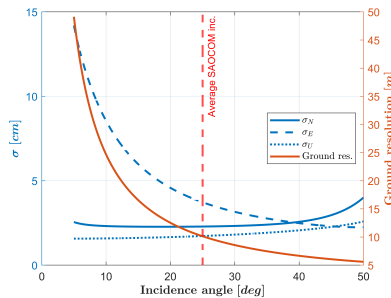


Figure 9: Incidence angle tradeoff, with atmosphere, 200 m baseline - Cryosphere scenario.

A detailed examination of the **incidence angle trade-off** (which way of reasoning is highlighted in 12) is conducted across various scenarios, providing practical insights for optimal InSAR system design. As the incidence angle increases, both SNR and accuracy decrease, while ground resolution improves. The impact of the rotation matrix is crucial, contributing to enhanced accuracy in specific scenarios.

$$\theta^{(i)} \rightarrow \sigma_0^{(i)} \rightarrow \text{SNR}^{(i)} = \sigma_0^{(i)} - \sigma_{\text{NESZ}}^{(i)} \rightarrow \gamma^{(i)} = \dots \quad (12)$$

Finally, the introduction of the **orbital tube** concept is necessary. Two main baselines — low

(200 m) and high (1000 m) — are explored, representing realistic and threshold cases, respectively. The orbital tube, defined as a 99.73 % probability region and shown in Figure 10, is crucial in considering the uncertainty in satellite orbits.

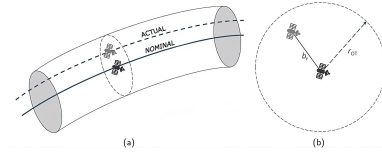


Figure 10: (a) provides a clear view of the orbital tube. (b) displays a cross-sectional view.

## 6. Multi-Passage Performances

The last part of the work is about the repeat-pass bistatic InSAR system analysis.

First of all, three distinct scenarios are meticulously examined: Solid Earth, Cryosphere, and Short Vegetation. In this case, Landslides analysis is not useful because now the deformation rate is assessed. In fact, the focus now lies on LoS velocity estimation, with considerations for atmospheric effects, topography, and decorrelation phase noise, where the **Hybrid Cramér–Rao Bound (HCRB)** replaces the Cramer-Rao Bound [3], setting a lower limit for parameter estimation performance.

This time, it is more useful to write the System 13 aligning all the active and then the passive phases.

$$\begin{bmatrix} \varphi_1^a \\ \vdots \\ \varphi_n^a \\ \varphi_1^p \\ \vdots \\ \varphi_n^p \end{bmatrix} = \mathbf{A} \begin{bmatrix} v_x \\ v_r \end{bmatrix} \quad (13)$$

where

$$\mathbf{A} = \frac{2\pi}{\lambda} \begin{bmatrix} 0 & 2t_1 \\ \vdots & \vdots \\ 0 & 2t_n \\ t_1 \sin \phi_{bs} & t_1(1 + \cos \phi_{bs}) \\ \vdots & \vdots \\ t_n \sin \phi_{bs} & t_n(1 + \cos \phi_{bs}) \end{bmatrix}$$

Robust parameter estimation methods, particularly Least Squares (**LS**, see Equation 14) and

Best Linear Unbiased Estimator (**BLUE**, see Equation 15) are showcased for their reliability in the face of environmental disturbances. Both LS and BLUE methods perform well when evaluating accuracies. Nonetheless, BLUE performs way better when a lot of time passes.

$$\hat{\mathbf{v}}_{\text{LS}} = \mathbf{A}^\dagger \boldsymbol{\varphi} = (\mathbf{A}^H \mathbf{A})^{-1} \mathbf{A}^H \boldsymbol{\varphi} \quad (14)$$

$$\hat{\mathbf{v}}_{\text{BLUE}} = \mathbf{B} \boldsymbol{\varphi}, \quad \mathbf{B} = (\mathbf{A}^H \mathbf{C}_{\mathbf{w}}^{-1} \mathbf{A})^{-1} \mathbf{A}^H \mathbf{C}_{\mathbf{w}}^{-1} \quad (15)$$

At this point, a randomized baseline is introduced in the performance tool. This dynamic approach offers a more realistic representation of baseline variations, providing valuable insights into the system's performance under changing conditions. Randomization of the baseline considering a low baseline case ( $b = 200$  m) is introduced. The outcomes across nearly all scenarios exhibit very good performance, demonstrating a remarkable level of accuracy achieved, typically in the range of 2 – 3 cm/year after 1 year. This is exemplified in the Cryosphere scenario, as illustrated in Figure 11.

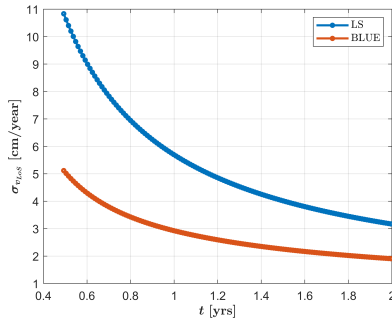


Figure 11: Accuracy on LoS velocity, Cryosphere scenario, time span of 1.5 years, **atmosphere + decorrelation phase noise** considered.

In comparing LoS velocities with and without topography, both the LS and BLUE methods converge after about a year, showing negligible differences in outcomes (see Figure 12). This convergence is attributed to the topography's diminishing influence over time. Moreover, the topography becomes effectively estimable as a parameter due to equation sufficiency, mainly due to the  $\mathbf{k}_z$  vector misalignment with the time vector in the various scenarios.

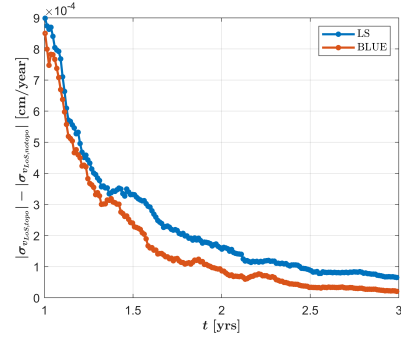


Figure 12: Difference on LoS velocity with and without topography, Solid Earth scenario, time span of 2 years, from 1 to 3 years.

The sustained estimation of Digital Elevation Model (DEM) parameters over years, despite a challenging 2-year timeframe, is demonstrated in Figure 14. However, stabilization of DEM estimation at  $\sigma_{topo} \approx 2.8$  m requires a 5-year period. To reduce plot noise, DEM values underwent 100-time averaging, every time using different baseline vectors (thus, different  $\mathbf{k}_z$  vectors). Using a single baseline from `normrnd` would capture specific instances, influenced by unique random phenomena, resulting in noisy plots, as in Figure 13.

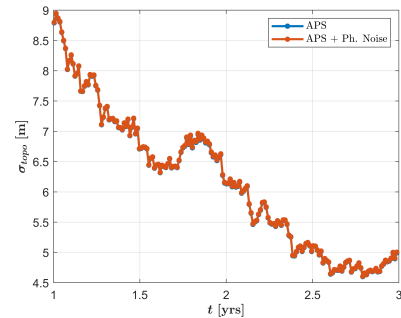


Figure 13: Topography estimation, Cryosphere scenario, not averaged.

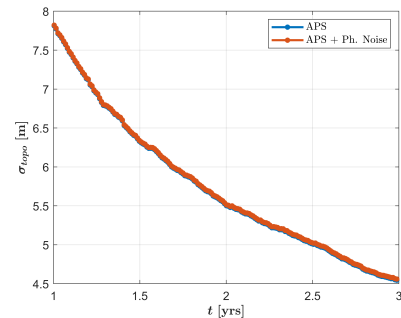


Figure 14: Topography estimation, Cryosphere scenario, **averaged 100-times**.

## 7. Conclusion and Future Developments

The work reveals critical insights into bistatic InSAR system dynamics. The single-pass analysis emphasizes the trade-off between accuracy, incidence angle, and ground resolution, noting the impact of atmospheric effects and phase noise. The rotation matrix and consideration of an orbital tube, representing a 99.73 % probability region for satellite orbits, are identified as key determinants of accuracy. The repeat-pass analysis considers scenarios with topography, finding negligible influence on LoS velocity estimation. The BLUE method outperforms the LS method, and baseline randomization within the orbital tube introduces complexity. In essence, the research underscores the need to balance parameters for optimal system performance.

Looking ahead, future research should address complex scenarios, refine orbital tube dynamics, validate against real-world data, and explore a broader range of orbital parameters. The developed system serves as a bridge between current and future SAR missions, offering both Level 2 products and pioneering observation capabilities. In seismic regions, the BiSAR system complements existing spaceborne missions, contributing significantly to a comprehensive understanding of seismic motion.

## References

- [1] ESA. Saocom-cs mission science document. Eop-sm/2764/, ESA, 2015.
- [2] Africa Ixmucane Flores-Anderson, Kelsey E. Herndon, Rajesh Bahadur Thapa, and Emil Cherrington. *THE SAR HANDBOOK: Comprehensive Methodologies for Forest Monitoring and Biomass Estimation*. SERVIR Global Science Coordination Office, 2019. First edition. Published electronically April 2019. DOI: 10.25966/nr2c-s697.
- [3] Andrea Monti Guarnieri and Stefano Tebaldini. On the exploitation of target statistics for sar interferometry applications. *IEEE Transactions on Geoscience and Remote Sensing*, 46(11):3436–3443, 2008.
- [4] Stefano Tebaldini, Christian Barbier, et al. Parsifal: Passive/active radar spaceborne imaging for applications at l-band. Proposal prepared in response to the revised ESA EE9 call.
- [5] Fawwaz Ulaby, M. Craig Dobson, and José Luis Álvarez Pérez. *Handbook of Radar Scattering Statistics for Terrain*. 2019.